

SDSS-IV MANGA: IONIZATION SOURCES OF DIFFUSE EXTRA-PLANAR GALACTIC MEDIUM

© 2023 VERA K. POSTNIKOVA ^{1,2}^a, DMITRY BIZYAEV ^{3,1}

¹Sternberg Astronomical Institute, Lomonosov Moscow State University, Moscow, Russia

²Physics Department of Lomonosov Moscow State University, Moscow, Russia

³Apache Point Observatory and New Mexico State University, Sunspot, NM, 88349, USA

ABSTRACT

We explore sources of ionization of diffuse gas at different altitudes in galaxies in dependence of their stellar mass, H α luminosity, and specific star formation rate. We use the MaNGA data from SDSS-IV data release DR16 together with photoionization and shock ionization models provided by the 3MdB database. Our sample comprises 239 edge-on galaxies, which makes our results statistically valuable. We reach very high galactic altitudes with the help of spectra stacking. We demonstrate that models of the gas photoionization in a combination of young OB-stars and hot low-mass evolved stars (HOLMES) describes the gas ionization state in the galaxies of all types on diagnostic diagrams. Nevertheless, the shock waves may contribute to the gas ionization in massive galaxies with passive star formation. We observe a general trend of decreasing the fraction of the ionizing flux from OB-stars and the ionization parameter with the altitude, while the role of the ionization by the HOLMES increases. The biggest difference in the contribution from these types of ionizing sources correlates with the specific star formation rate and with stellar masses of galaxies. The HOLMES are the principal gas ionization sources in massive galaxies with passive star formation, while OB-stars dominate the gas ionization in low-mass galaxies with active star formation.

Keywords: galaxies: diffuse ionized gas – ISM galaxies: optical spectroscopy – spiral galaxies – modeling

INTRODUCTION

Hoyle & Ellis (1963) started investigating the diffuse ionized gas medium (DIG) in the Milky Way galaxy, which lead to its detection not only in the galactic midplane, but also at high galactic altitudes (Reynolds et al. 1973). Later, the DIG was discovered in other galaxies (Dettmar 1990; Rand et al. 1990). It was found that the DIG phase prevails at several kpc above the galactic midplane (Reynolds 1991). A decade ago kinematics of the neutral (Swaters et al. 1997; Marasco et al. 2019) and ionized gas (Rand 2000) was quite well studied only in a few nearby galaxies. Recent progress in massive multi-object spectral extragalactic surveys enables us to study kinematics of ionized gas in and around objects of the local Universe for statistically large samples of galaxies (Bizyaev et al. 2017; Levy et al. 2019; Bizyaev et al. 2022).

At the same time the ionization sources of the extraplanar gas at large galactic altitudes (eDIG hereafter) are still not well understood for our and other galaxies. Thus, the ionizing photons flux from the OB-stars in the galactic midplane is sufficient to explain the amount of ionized gas in galaxies with active star formation (Haffner et al. 2009; Flores-Fajardo et al. 2011). On the other hand, the bright forbidden line ratios at high galactic altitudes in some galaxies require taking into account evolved stars as the main source of the gas ionization (Flores-Fajardo et al. 2011; Zhang et al. 2017; Jones et al. 2017). The shock wave ionization was also proposed as a scenario for the explanation of the eDIG emission (Collins & Rand 2001).

A large data release DR16 (Ahumada et al. 2020) of the Mapping Nearby Galaxies at the Apache Point Observatory

^a E-mail: vraeranaz@gmail.com

(MaNGA, Bundy et al. (2015)), a part of the Sloan Digital Sky Survey-IV (SDSS-IV, York et al. (2000); Blanton et al. (2017)) allows us to make a large sample of objects with convenient to observe eDIG. Due to a large number of galaxies, with the help of spectra stacking we can trace eDIG to extremely large altitudes above the galactic midplane — up to a dozen kpc. The main purpose of this study is to advance the eDIG studies with the new, large MaNGA sample and new spectra modeling results.

In the next section we describe the MaNGA data that we utilize and their analysis. Then we describe the used diagnostic diagrams and the line ratio modeling. Then we report our results and discuss them. Finally, we summarize our results. We assume that the Hubble constant is $70 \text{ km s}^{-1} \text{ Mpc}^{-1}$ throughout our paper.

SDSS-IV MANGA DATA

THE MANGA SPECTRA

We employ data from the MaNGA survey released in the frames of DR16 of SDSS-IV. The MaNGA survey was conducted with the 2.5-m Sloan telescope (Gunn et al. 2006) at the Apache Point Observatory with the resolution of $R \sim 2000$ and in the wavelength range of 3600–10300Å (Smeed et al. 2013). The survey followed a sample of over 10,000 galaxies with a uniform distribution by stellar mass at the median redshift of $z \approx 0.03$ (Wake et al. 2017).

The MaNGA obtained resolved two-dimensional spectral maps for its objects via two fiber-fed spectrographs (Smeed et al. 2013) with the Integral Field Unit (IFU) heads (Drory et al. 2015) that consisted of densely packed optical fibers allocated at the telescope’s focal plane. The fiber projection diameter was 2 arcsec, and the spatial filling factor for the packed circular fibers was 56%. The full coverage of observed objects was realized via a 3-point dithering, which allowed to restore continuous spectra images, see Law et al. (2015).

The MaNGA data reduction pipeline consists of two main stages. The first stage is the Data Reduction Pipeline (DRP, Law et al. (2016)), which delivers flux-calibrated spectra cubes homogenized to the uniform angular resolution of about 2.5 arcsec (FWHM) placed on a regular rectangular spatial grid with a 0.5 arcsec spaxel. The photometric calibration precision was not worse than 5% (Yan et al. 2016a,b). The second stage is the Data Analysis Pipeline (DAP, Westfall et al. (2019)), that separated the absorption and emission spectra using the Penalized Pixel Fitting (pPXF) method (Cappellari & Emsellem 2004; Cappellari 2017), which allowed one to estimate global parameters of galaxies, to obtain two-dimensional maps of various astrophysical parameters, cubes of co-added binned spectra, and best-fitting model spectra.

We make use of the cubes of emission spectra obtained after subtracting the model continuum from the observed spectra, maps of some emission line fluxes, and gas velocity maps out of the MaNGA products. We also use some global parameters derived from published SDSS photometry.

MAKING MASKS FOR SELECTED GALAXIES

We create spaxel masks to select only good quality data for the consequent spectra stacking. We leave only spaxels that satisfy the following criteria:

- the emission spectrum was successfully modeled for this spaxel, with no bad data processing flags;
- the radial velocity in the $H\alpha$ emission line was successfully determined for this spaxel, with no bad data processing flags;
- the signal-to-noise ratio (SNR) in the $H\alpha$ line was ≥ 3.0 ;
- the absolute value of the radial velocity for this spaxel was within 350 km s^{-1} of the galactic center velocity.

ANALYSIS OF THE SAMPLE

The primary selection of edge-on galaxies was performed via the visual inspection of composite, color images made by SDSS survey. Our experience in selecting edge-on objects for large catalogs (Bizyaev et al. 2014) and for individual studies of MaNGA objects (Bizyaev et al. 2017) shows that the visibility of the dust lane projected to the central region of galaxies suggests high inclinations of galactic midplane to the line of sight $\geq 85^\circ$, which also has been confirmed with calculations by Bizyaev & Kajsın (2004); Mosenkov et al. (2015). In turn, the high inclination ensures that we can study highly elevated gas without its overlapping on bright star formation regions in the midplanes of galaxies. Our result of the visual selection is a sample of 258 edge-on galaxies.

After the visual inspection we notice that some galaxies should be rejected based on their maps of the $H\alpha$ emission, maps of the equivalent width $EW(H\alpha)$, and maps of the stellar and gas velocities. Thus, our sample has a few objects

in which their gas and stars rotate in near orthogonal planes, which resembles galaxies with polar rings, see e.g. [Moiseev et al. \(2011\)](#). While they can be interesting objects for the further studies, they don't allow us to study eDIG by the methods that this paper uses. As a result, we reject 32 more galaxies that have one or more of the following features:

- a large angle between the stellar and gas rotation;
- evident inconsistency between reported photometric parameters and observed picture, e.g. when the effective radius R_{eff} is too large with respect to the visible size of the object;
- the spaxel mask rejects the majority of galactic regions, which can statistically bias the contribution of the remained spaxels from this object to the stacked spectra.

The resulting sample comprises 239 galaxies. We show them as a mosaic in Figure 1.

THE SPECTRA STACKING PROCEDURE AND THE EMISSION LINE FLUX ESTIMATION

Since we study faint regions far away from galactic midplanes, the individual SNR of their emission lines is often too low for the analysis. To increase the SNR, we stack spectra from regions that are close by their properties. To do it, we subdivide the sample by a small number of groups, or bins, with relatively similar global parameters. Among with studying the eDIG properties at different altitude bins, we also incorporate a binning by the following galactic parameters:

- the integral stellar mass M_s estimated by the NASA-Sloan Atlas of galaxies (NSA¹);
- the galactic luminosity not corrected for the reddening $L_{H\alpha-R_{eff}(r)}$, which is the $H\alpha$ luminosity within one effective radius R_{eff} in the r -band, and proportional to the star formation rate (SFR), and also taken from the NSA;
- the specific star formation rate $sSFR$ estimated as $sSFR = L_{H\alpha-R_{eff}(r)}/10^{41.27}/M_s$, where the normalization is derived by [Kennicutt & Evans \(2012\)](#), [Murphy et al. \(2011\)](#), [Hao et al. \(2011\)](#);
- the visual altitude of spaxels z/z_0 above the galactic midplane normalized by the exponential scale height, the latter was estimated as $z_0 = 0.596 \cdot R_{eff} \cdot b/a$, where R_{eff} is the effective radius, and b/a is the minor-to-major axis ratio from a 2D fitting in the r -band, both taken from the NSA estimated in the r -band with the Petrosian parameterization.

We optimize the binning via selecting the number of bins and their borders in the way that in each bin by the galactic parameters and by the altitude has a contribution from at least 10% of all galaxies in the sample. After that we co-add corrected for the radial velocities emission spectra in each bin. We ensure that the corrected spectra have no other lines within $\pm 7.5\text{\AA}$ from the line of interest. We also check and confirm that the DAP subtracted continuum spectra so well that an additional continuum correction is not required. The flux in selected emission lines is found via a simple integration of the line intensity profiles within $\pm 7.5\text{\AA}$ from the line centers. Then we correct the line fluxes for the extinction based on the Balmer decrement. Since the DAP provides uncertainties of the emission intensities in each spaxel, we find the resulting flux uncertainties via the standard error propagation method.

As a result, we co-add the emission spectra for 239 galaxies in the optimal bins by the general galactic parameters and by the galactic altitude according to the procedure described above. Then we find the emission line fluxes and their uncertainties. An example of our binning by the galactic altitudes is shown in Figure 2.

DIAGNOSTIC DIAGRAMS AND THEORETICAL MODELS

DIAGNOSTIC DIAGRAMS

In order to compare the data of observations with models, we employ diagnostic diagrams that are based on relative intensities of emission lines. They enable us to efficiently separate regions with different physical conditions. The diagnostic diagrams are widely used after a study by [Baldwin et al. \(1981\)](#), where the advantage of two-dimensional

¹ <http://nsatlas.org>

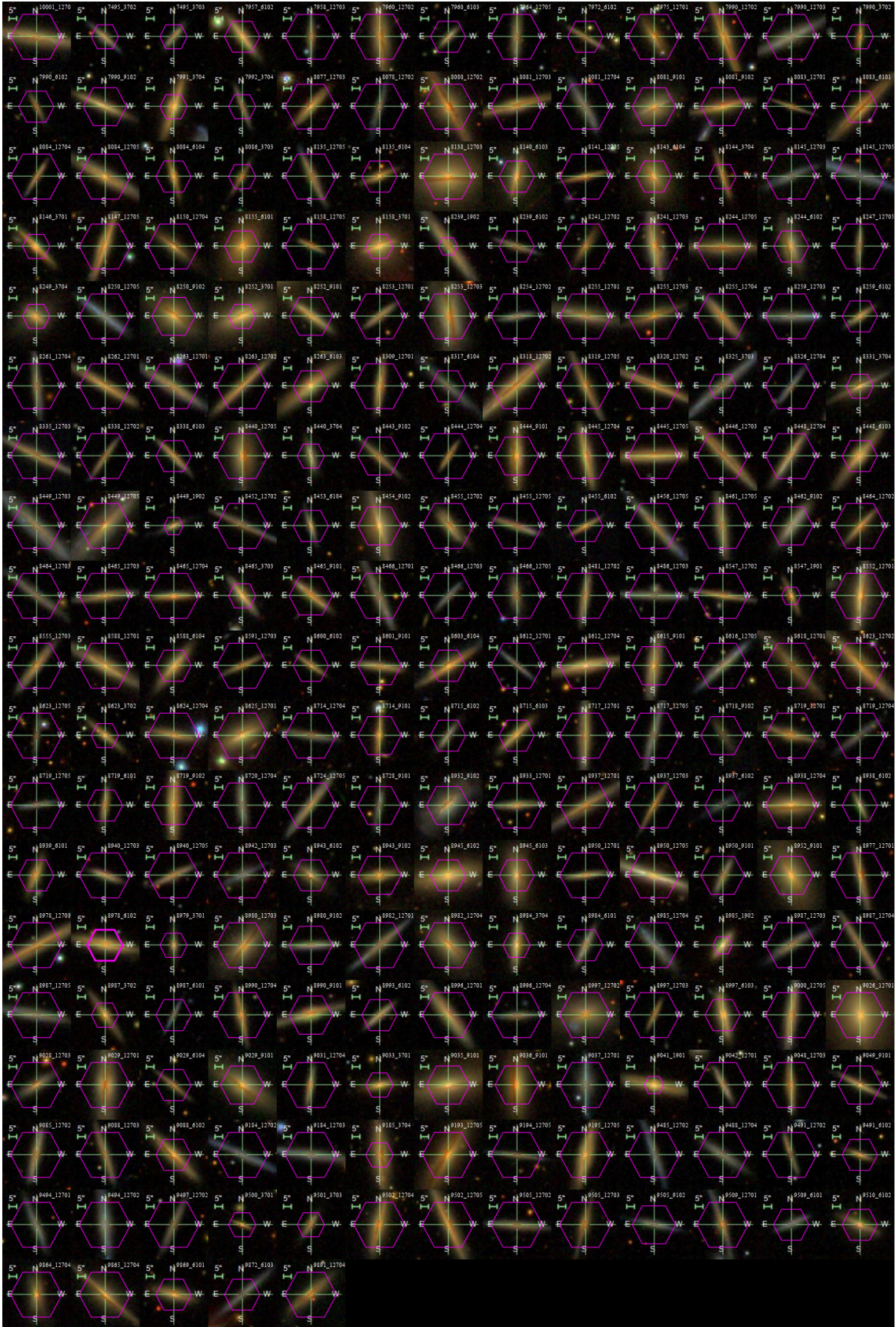


Figure 1. The mosaic of 239 galaxies from our sample. The magenta hexagons that designate the MaNGA IFU coverage overlap on SDSS color images.

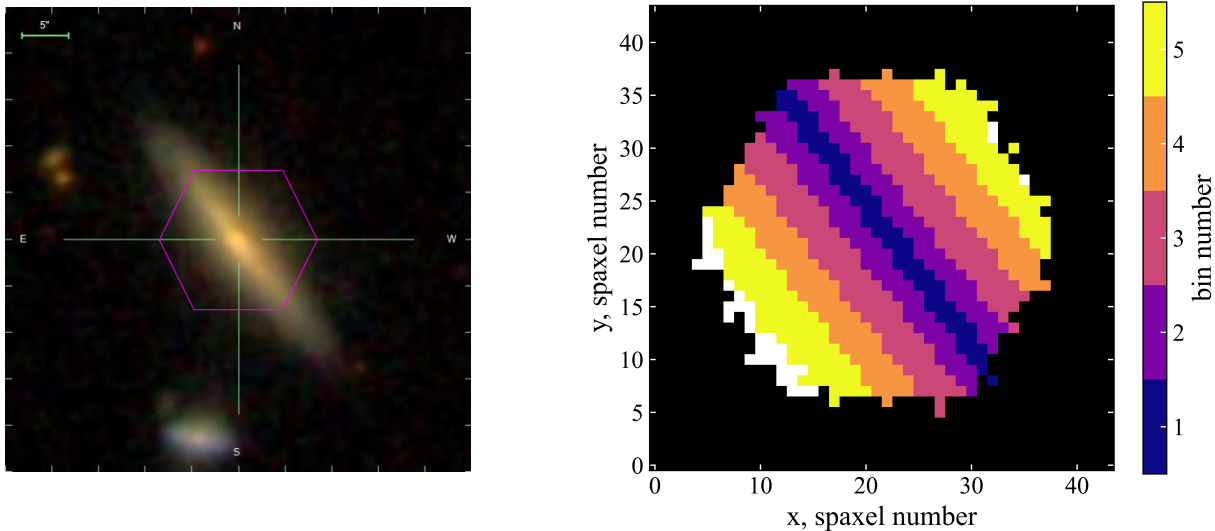


Figure 2. Left: an SDSS image of one of our galaxies with superimposed IFU area outlined by the magenta hexagon. Right: corresponding bins by the galactic altitude with the spaxel mask shown by the white color.

classification was demonstrated and also the most useful combinations of strong emission lines were introduced. [Veilleux & Osterbrock \(1987\)](#) also considered a set of the line ratios on diagnostic diagrams, and both works contributed to a set of the diagrams that are traditionally called as BPT-diagrams. [Dopita et al. \(2000\)](#) explained and updated the classification with the help of models that described the gaseous medium.

An important addition to the diagnostic diagrams are the demarcation lines, which show borders between the gas with different ionization mechanisms. The most frequently used demarcation lines were introduced by [Kewley et al. \(2001\)](#), [Kauffmann et al. \(2003\)](#), [Kewley et al. \(2006\)](#). A more advanced approach to the demarcation line setting that utilizes gas dynamics was considered by [Law et al. \(2021\)](#). The data of MaNGA allow us to use a variety of emission line combinations for the diagnostic diagrams, but in this work we limit the study by 3 traditional BPT diagrams:

- $\log([\text{OIII}]\lambda 5007/\text{H}\beta)$ vs $\log([\text{NII}]\lambda 6583/\text{H}\alpha)$;
- $\log([\text{OIII}]\lambda 5007/\text{H}\beta)$ vs $\log([\text{SII}]\lambda\lambda 6716, 6731/\text{H}\alpha)$;
- $\log([\text{OIII}]\lambda 5007/\text{H}\beta)$ vs $\log([\text{OI}]\lambda 6300/\text{H}\alpha)$.

THE 3MDB MODELS

The models of the gas ionization based on numerical computations are widely demanded for studies of interstellar medium. At the same time, running the computations is a time-consuming process, and they are run and published mostly for limited and specific cases. This problem was mitigated by the creation of the Mexical Million Models dataBase (3MdB) by [Morisset et al. \(2015\)](#) and [Alarie & Morisset \(2019\)](#). The 3MdB contains pre-computed model emission line ratios that are organized as a MySQL database. This approach allows one to save time and computation resources and simplifies comparison between observations and modeling.

At the moment the 3MdB consists of two major parts:

- The database of photoionization models 3MdB-p ([Morisset et al. 2015](#)) computed with the package Cloudy ([Ferland et al. 1998](#)), version C13 ([Ferland et al. 2013](#)). This database considers several principal setups of the photoionization modeling and includes the grids "DIG_HR" — the models designed for the DIG (and eDIG) description. They assume that the gas is ionized by a combination of radiation from OB-stars and from HOT Low-Mass Evolved Stars (HOLMES). The choice of these two main sources of the gas ionization is based on a study of a well-known edge-on galaxy NGC 891 ([Flores-Fajardo et al. 2011](#)). One of the purposes of our study is to verify whether the generalization of this assumption is suitable for all types of galaxies.

- The database of shock ionization models 3MdB-s (Alarie & Morisset 2019) computed with the help of the MAPPINGS astrophysical plasma modeling code (Binette et al. 1985), version V (Sutherland et al. 2018). Out of cases considered by this set of models, the most relevant are the models "Allen08" described by Allen et al. (2008). Another goal that we pursue in this paper is to verify whether the shock models can be relevant to the ionization of gas at different galactic altitudes in various types of galaxies.

THE PHOTOIONIZATION MODELS "DIG_HR"

The photoionization grids, that describe the diffuse gas in the frames of the 3MdB-p database, have 4 model parameters.

1. The flux from the OB-stars Φ_{OB} , *photons/sec/cm²*. It spans the range $\log \Phi_{OB} = (3.5 \div 7.5)$ with the step of 0.25 dex.
2. The ionization parameter $U = \Phi_{total}/n_e/c$, where $\Phi_{total} = \Phi_{OB} + \Phi_{HOLMES}$, n_e is the electron density, and c is the speed of light. It spans the range $\log U = (-4.0 \div -3.0)$ with the step of 0.1 dex.
3. The gas metallicity O/H defined as the ratio of the number of corresponding atoms. It spans the range $\Delta O/H = (-1.0 \div 0.6)$ with the step of 0.1 dex, where $\Delta O/H + 8.69 = 12.00 + \log O/H$.
4. The nitrogen abundance N/O defined as the ratio of the number of corresponding atoms. It spans the range $\log N/O = (-1.4 \div -0.2)$ with the step of 0.1 dex.

It is important to notice that the HOLMES flux is fixed at $\Phi_{HOLMES} = 8.4 \cdot 10^4$ *photons/sec/cm²* in all "DIG_HR" models. All other metal abundances relative to O are fixed to the solar values except for the Mg, Si, and Fe, which are decreased by 1 dex with respect to the solar values.

THE SHOCK MODELS "ALLEN08"

The grids of models for the shock ionization "Allen08" have also 4 model parameters:

1. Pre-shock gas density. We consider only two realistic in our case values: $n = 0.1$ *cm⁻³* and $n = 0.01$ *cm⁻³*.
2. The gas metallicity. We have to stick to the solar metallicities for these grids because the lower metallicity cases, e.g. typical for the Large and Small Magellanic Clouds, are not computed for very low gas densities typical for the eDIG. We analyze possible behavior of the models for the eDIG set of parameters below.
3. The magnetic field. In the midplane of our and other galaxies the magnetic field has $B \simeq 10$ μG , which decreases with the altitude down to $B \simeq 5$ μG at several kpc above the midplane. We consider a range of the B between 1 and 10 μG . Within this range the "Allen08" grids are computed for the $B = (1.0, 1.26, 1.58, 2.0, 3.16, 4.0, 5.0, 10.0)$ μG with $n = 0.1$ *cm⁻³* and for the $B = (1.0, 10.0)$ μG with $n = 0.01$ *cm⁻³*.
4. The shock wave velocity. We consider all provided values of this parameter. For the grids with $n = 0.1$ *cm⁻³* the velocities range between 100 and 1000 *km s⁻¹*, and with $n = 0.01$ *cm⁻³* they range between 200 and 1000 *km s⁻¹*, both with the step of 25 *km s⁻¹*.

RESULTS

THE OPTIMALITY OF OUR BINNING

Our binning scheme fills all altitude bins with statistically valuable number of representatives. When only the altitude binning is considered, about 30% of all galaxies contribute to the highest, least populated bin. When an additional galaxy parameter binning is added, some 10% of all galaxies have representative data in the highest bin.

We ensure that our binning scheme is stable against the number of galaxies in the parental sample, the number of altitude bins, and the bin altitude border values by changing these values and inspecting the resulting diagrams explained below.

CO-ADDED GALACTIC SPECTRA IN THE DIAGNOSTIC DIAGRAMS

Here we consider how the line ratios of our co-added spectra overlap with the model photoionization and shock grids in dependence of our integral galactic parameters M_s , $L_{H\alpha-R_{eff}(r)}$, and $sSFR$. Note that we vary the $\Delta O/H$ and $\log N/O$ for the photoionization models in dependence on galactic parameters, which is discussed below. The results are shown in Figures 3, 4, and 5.

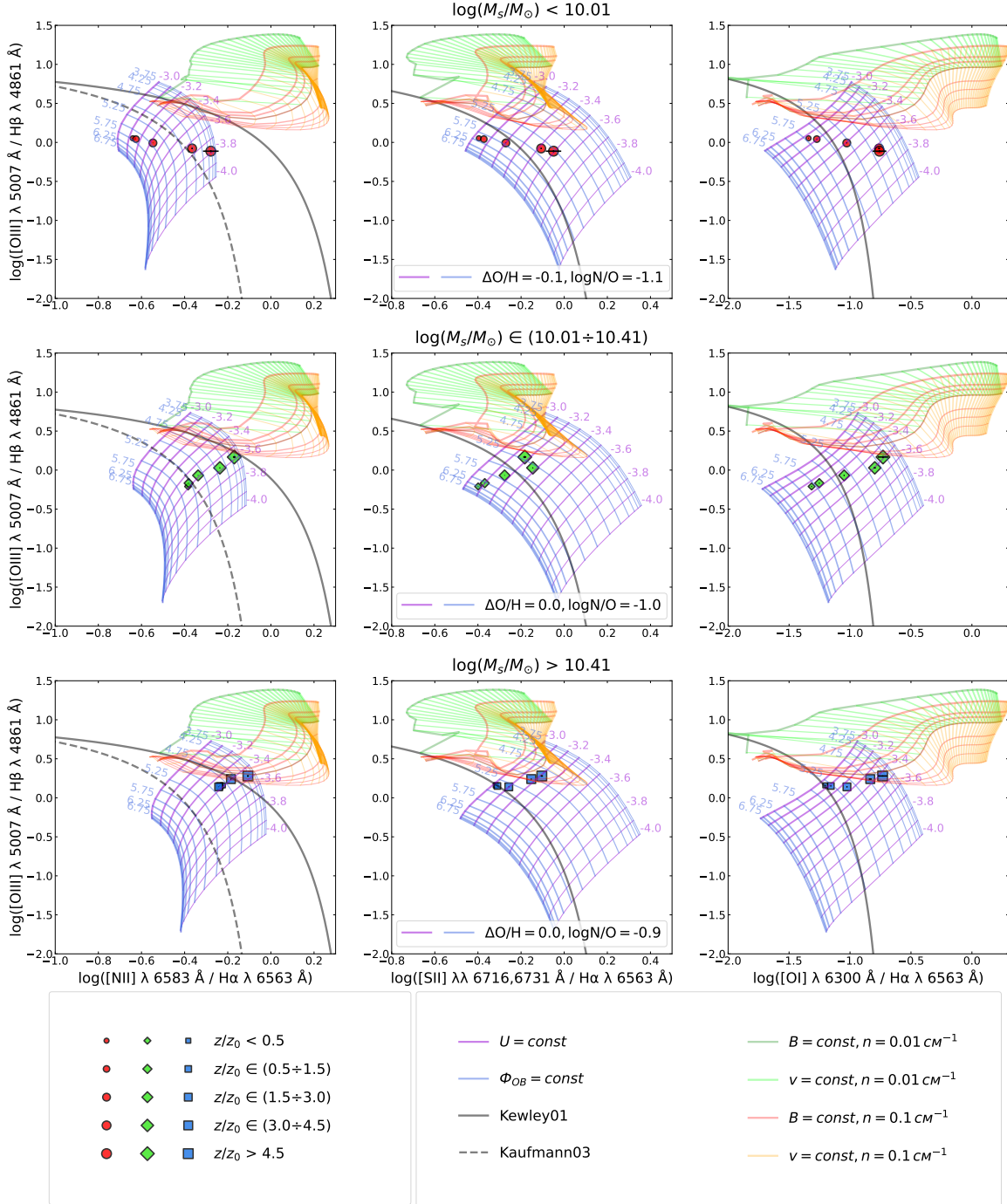


Figure 3. BPT-diagrams with our observing flux ratios shown for different altitude and stellar mass M_s bins. The bigger symbol size corresponds to a higher altitude. The red circles, green rhombuses and blue squares designate the lower, intermediate, and higher bins in the M_s , respectively. The model photoionization (blue) and shock (red and green) grids (see text) are also shown. The thicker lines designate the greater values of the corresponding parameter. Since we are focused on the former models, the shock grids are shown for comparison purposes and their parameters are not specified in the plot. The demarcation lines from Kewley et al. (2001) and Kauffmann et al. (2003) are plotted with the solid and dashed curves, respectively.

THE DATA INTERPOLATION ON THE DIAGNOSTIC DIAGRAMS

As we can see in Figures 3–5, some high-altitude data for the intermediate and high M_s , for the low and high $L_{H\alpha-R_{eff}(r)}$ and for low and intermediate $sSFR$ fall onto the cross-section of the photoionization and shock grids. Nevertheless, all our observing line ratios can be explained with the photoionization grids only. The position of the points on the BPT diagrams can be translated to the OB-stars relative flux and the ionization parameter via a

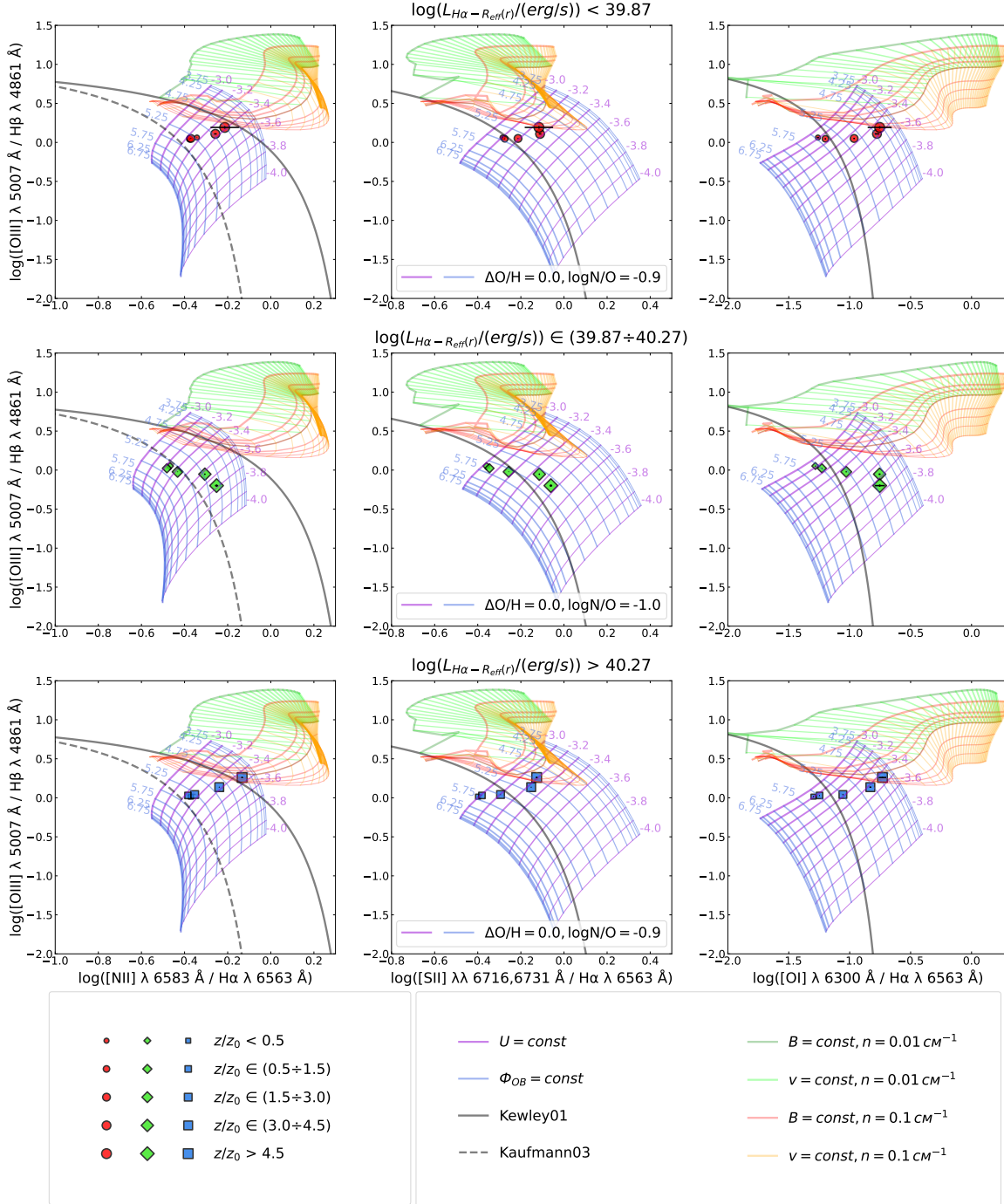


Figure 4. BPT-diagrams with our observing flux ratios shown for different altitude and $L_{H\alpha - R_{eff}(r)}$ bins. All designations are kept the same as in Figure 3.

grid interpolation procedure. Below we estimate these parameters by neglecting the shocks contribution to the gas ionization.

At the beginning, let's consider our simplest binning scheme by galactic altitudes only. We note that the O/H ratio should change with the altitude, but using photoionization models for HII regions from [Dopita et al. \(2016\)](#) we conclude that the O/H variation with the altitude can be neglected in the frames of the calibration uncertainties of ± 0.1 dex. When different BPT diagrams are compared between each other, the best agreement for our data can be achieved for $\Delta O/H = 0.0$ and $\log N/O = -0.9$, which corresponds to the solar abundance. Note that the models do not allow us to vary the S abundance, which leads to systematic bias of all diagrams that include the S. To avoid the bias, for the regression below we utilize only the BPT-plots based on H, N, and O. We also exclude the very

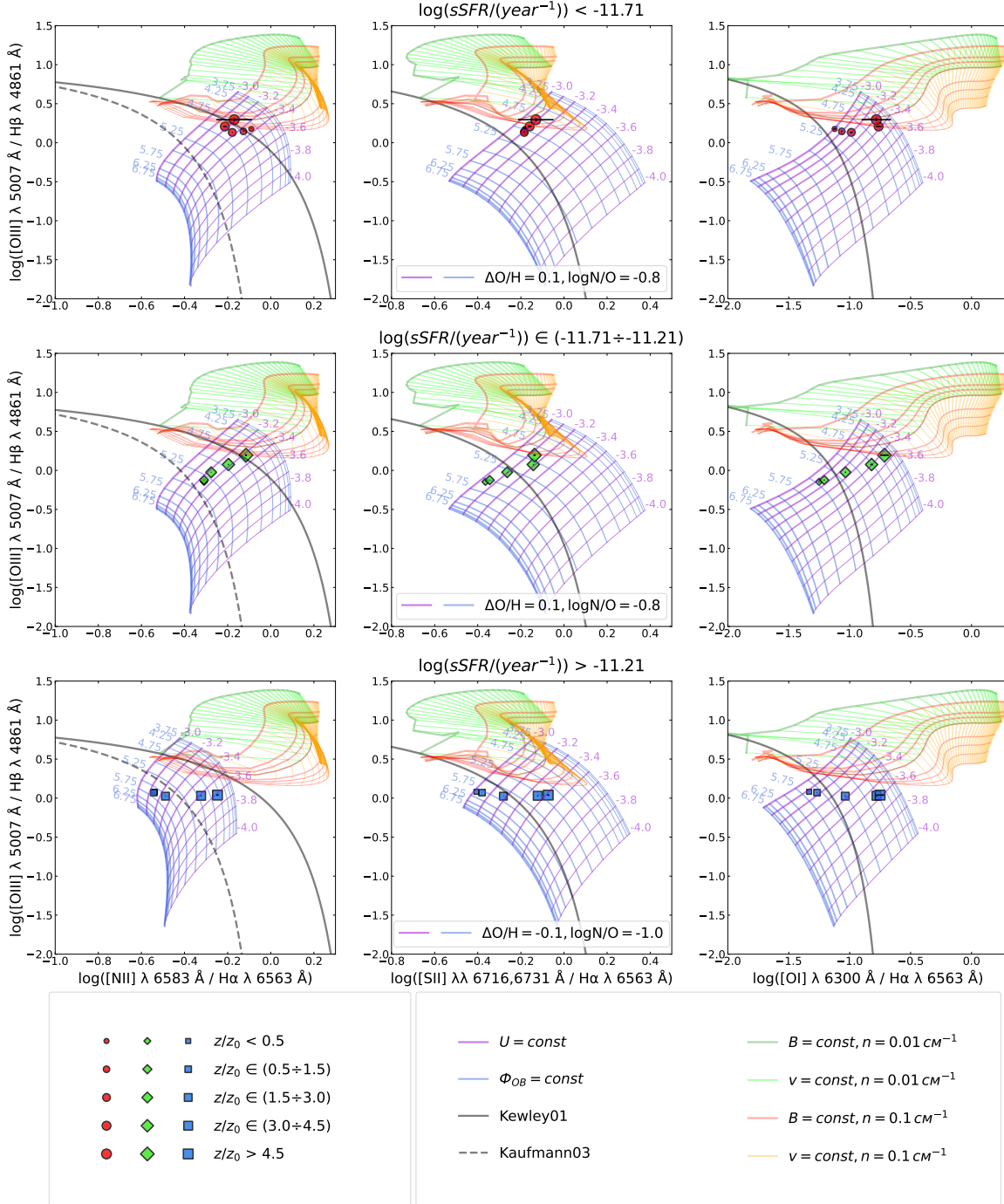


Figure 5. BPT-diagrams with our observing flux ratios shown for different altitude and $sSFR$ bins. All designations are kept the same as in Figure 3.

first, in-midplane bin from the further regression because a very high dust extinction there can bias line ratios even for nearby lines in spectra. The results of the grid interpolation and regression are shown in Figure 6.

Next, we consider more complicated binning cases and include additional galactic parameters introduced above. Before the interpolation, we also use results of HII regions modeling from [Dopita et al. \(2016\)](#) and ensure that the O/H ratio would not change by more than ± 0.1 dex in the case of the diagrams for case of adding the M_s , $L_{H\alpha-R_{eff}(r)}$, or $sSFR$ to the binning schemes, hence we conclude that we can neglect the O/H variation with the galactic altitude. Then we make the plots similar to Figure 6 that also include additional galactic parameters and find $\Delta O/H$ and $\log N/O$ for which the extracted parameters best agree between all our BPT plots.

We notice that the best values of $\Delta O/H$ and $\log N/O$ for the galaxies with different M_s (Figure 3) correlate with

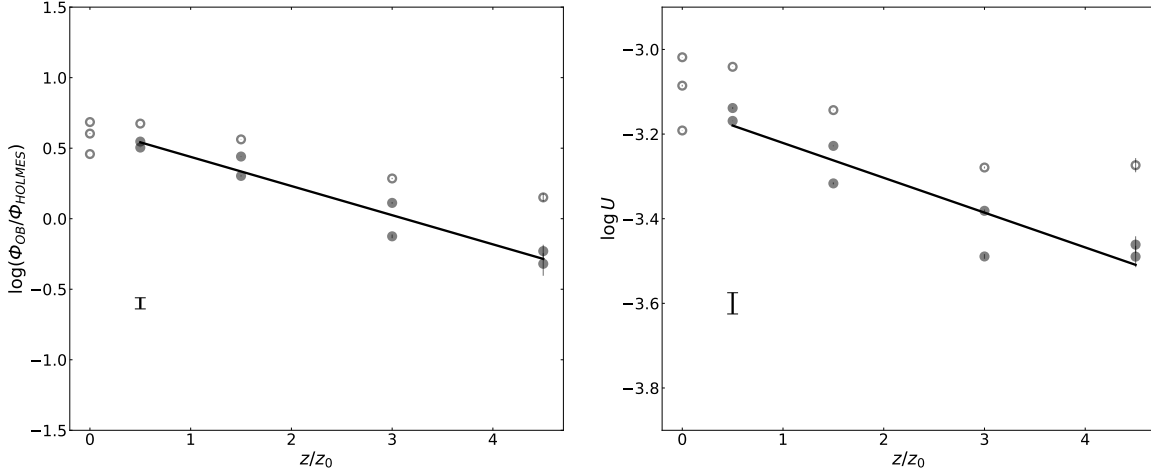


Figure 6. Results of the grid interpolation for the case of a general binning of all galaxies by the galactic altitude without involving any other galactic parameters. The ratio of OB-stars and HOLMES fluxes (left) and the ionization parameter (right) are shown with symbols, and the linear regression results are shown with lines. The error bars correspond to one sigma standard deviation. Open symbols are excluded from the regression (see text).

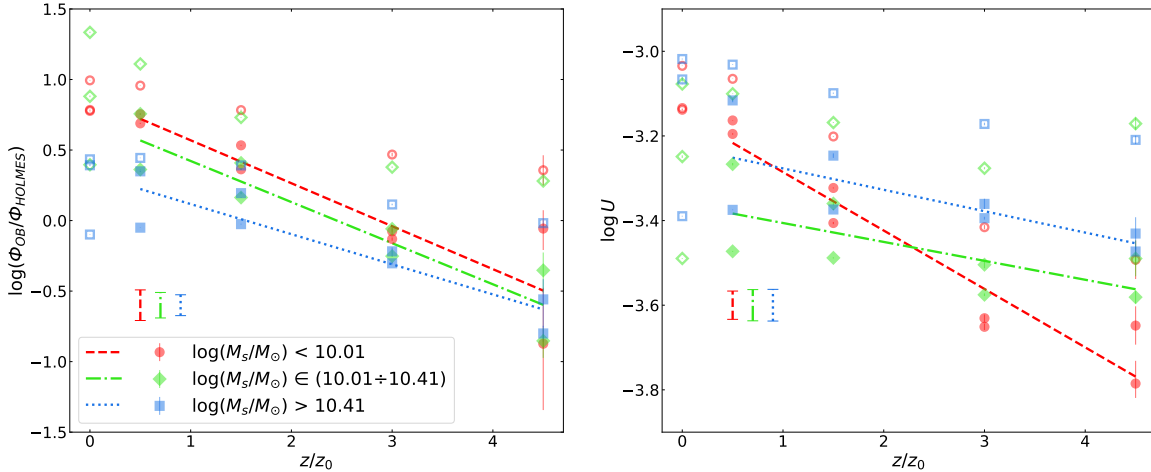


Figure 7. The altitudinal distributions of the extracted parameters, similar to Figure 6, but in this case the binning scheme includes stellar masses M_s . The red circles with dashed line, green rhombuses with dot-dashed line, and blue squares with dotted line designate the lower, intermediate, and higher bins in the M_s , respectively.

M_s same way as in well-known $O/H - M_s$ (see e.g. Tremonti et al. 2004; Andrews & Martini 2013; Curti et al. 2017), $N/O - M_s$ (Pérez-Montero & Contini 2009; Andrews & Martini 2013; Masters et al. 2016), and $N/O - O/H$ (Andrews & Martini 2013) relations.

As for Figure 6, we derive the best-fitting model parameters for each observing bin by interpolating among the model grids on the BPT diagrams. Then for the regression we include the BPT diagrams with H, N, and O only, and exclude the lowest galactic altitude points. The altitude distribution of the extracted parameters and the linear regression lines are shown in Figures 7–9.

DISCUSSION

Before making certain conclusion about possible contribution of shocks to the DIG ionization we need to verify how would the shock grids move in Figures 3–5 for the lower than solar gas metallicities, which is expected for eDIG at high galactic altitudes. As we have noticed above, grids for subsolar metallicities were computed in the 3MdB only with $n = 1 \text{ cm}^{-3}$, which is way higher than typical eDIG densities. Therefore, we consider the direction of trends for $n = 1 \text{ cm}^{-3}$ and assume that the trends will be the same for lower gas densities. The gas metallicities can be ordered as (1) twice as solar, (2) solar, (3) subsolar with the Large Magellanic Cloud values, and (4) subsolar with the Small Magellanic Cloud values. Comparing the model grids in this order, one can see that the shock grids move from the

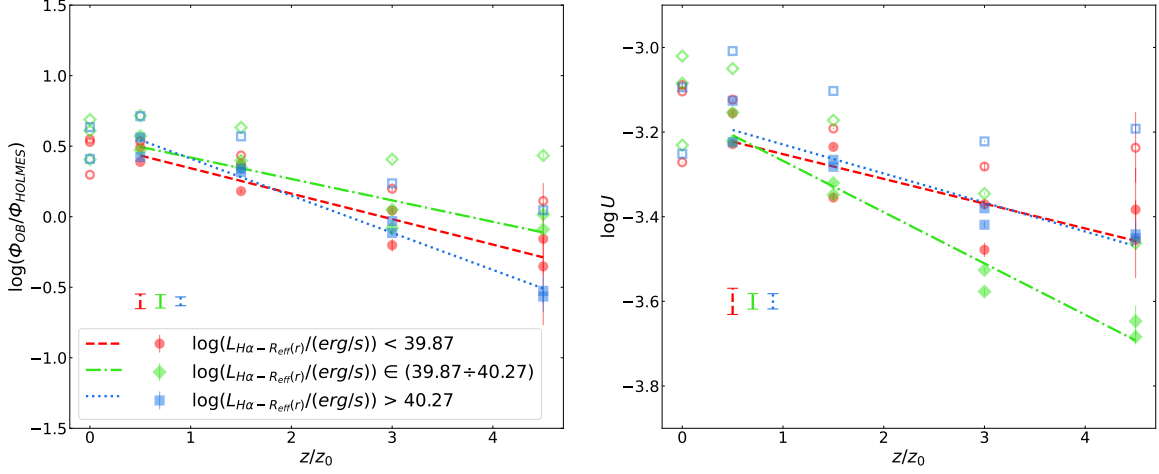


Figure 8. Same as Figure 7 for the case of binning by the $H\alpha$ luminosity within one R_{eff} in the r -band, $L_{H\alpha-R_{eff}(r)}$.

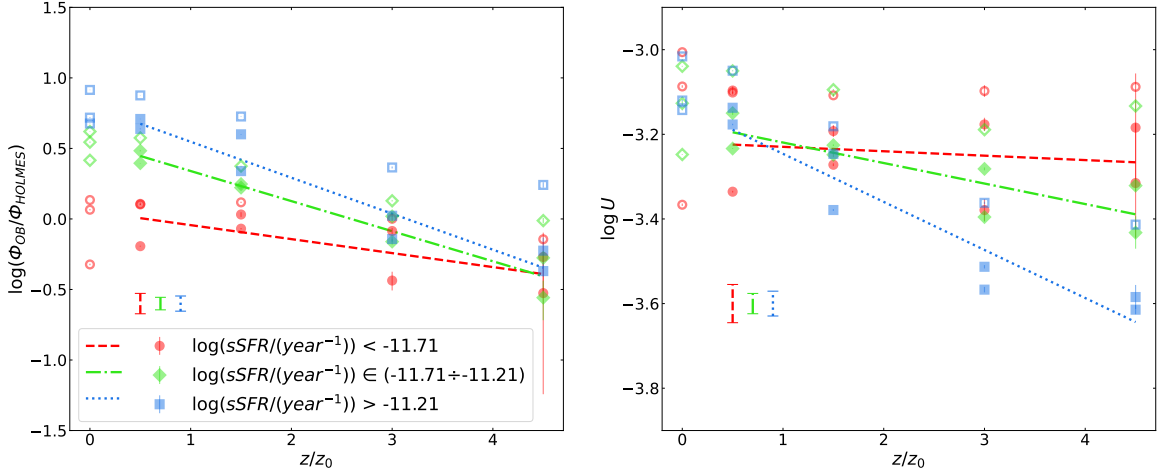


Figure 9. Same as Figure 7 for the case of binning by the $sSFR$.

right to the left in Figures 3–5, parallel to the abscissa axes. In this case the position of the shock grids on Figures 3–5 will not overlap more with the observing points and the conclusions are expected to remain the same for all low gas metallicities.

The eDIG emission line ratios on the BPT diagrams can be explained with two sources of ionization only: hot massive stars and HOLMES. This is important to stress that OB-stars alone cannot explain the line ratios in the eDIG at high altitudes, and incorporating HOLMES is required.

Nevertheless, we notice that some sets of parameters, like $z > 4.5 z_0$ for high and intermediate masses M_s (Figure 3), lowest and highest $L_{H\alpha-R_{eff}(r)}$ (Figure 4), or lowest and intermediate $sSFR$ (Figure 5) send observing points to the areas where the photoionization and shock grids overlap. This may suggest a non-negligible contribution of shock waves to the eDIG ionization in those types of galaxies.

As we remind above, the assumption of two types of sources (OB-stars and HOLMES) that ionize gas in the ”DIG-HR” photoionization models was based on the study by Flores-Fajardo et al. (2011) that relies on a single galaxy, NGC 891, in which the gas was traced up to 4 kpc above the galactic midplane. If we considered NGC 891 with its parameters from Rand et al. (1990), Shaw & Gilmore (1989), Karachentsev et al. (2013) as a part of our sample, it would fall into the high M_s bin, high $L_{H\alpha-R_{eff}(r)}$ bin, and intermediate bin by $sSFR$. Its altitudes z would span up to $(3 \div 4) z_0$. For comparison, parameters of the Milky Way from Robitaille & Whitney (2010), Licquia & Newman (2015), McMillan (2017) would place it to the high M_s bin, high $L_{H\alpha-R_{eff}(r)}$ bin, and intermediate $sSFR$ bin — similar to NGC 891.

We conclude that the assumption that eDIG on the BPT diagrams at any altitude in NGC 891 can be described

only by photoionization models made by Flores-Fajardo et al. (2011) is in agreement with our Figures 3–5. Therefore, the assumption about the OB-stars and HOLMES as the main sources of the DIG ionization based on a single galaxy, NGC 891, works well for the majority of other galaxies and for a wide range of galactic altitudes. Nevertheless, it does not take into account possible contribution from shocks, which reveals itself at the highest altitudes, in the most massive galaxies, and especially in galaxies with the lowest $sSFR$. Indeed, eDIG in our galaxies can be described by photoionization grids only, and we do not have to take possible contribution of shocks into account.

In a general case (Figure 6), we observe increasing contribution of HOLMES and decreasing contribution of OB-stars to the gas ionization with the galactic altitude. At low altitudes OB-stars contribute 3–5 times more to the ionization flux than HOLMES. At the highest altitudes, in a contrary, HOLMES contribute 2–3 times more to the gas ionization than OB-stars. The ionization parameter decreases systematically with the altitude. When the additional binning by the galactic parameters is applied, the trends described above are kept, qualitatively.

When the sample is additionally binned by stellar mass M_s (Figures 3 and 7), at any altitude the OB-flux contribution decreases when the mass increases. In the least massive galaxies the ionization parameter drops significantly with the altitude. The ionization parameter also increases with the mass at high galactic altitudes.

When the $H\alpha$ luminosity $L_{H\alpha-R_{eff}(r)}$ is used for the binning (Figures 4 and 8), at low galactic altitudes the OB-flux contribution increases with $L_{H\alpha-R_{eff}(r)}$, but this trend blurs at high altitudes.

In the case of $sSFR$ binning (Figures 5 and 9) we see the most clear difference between the two main sources of the gas ionization. At any galactic altitude increasing $sSFR$ means increasing contribution of OB-stars to the ionizing flux. Moreover, in the high $sSFR$ galaxies OB-stars contribute more than HOLMES at almost all galactic altitudes. Also the highest $sSFR$ galaxies demonstrate the most significant drop of the ionization parameter with altitude. In the low $sSFR$ galaxies the OB-stars contribution almost at all galactic altitudes is less than that of HOLMES. This contribution varies with the altitude slowly, as well as the ionization parameter does.

This study is a logical extension of the work by Jones et al. (2017), which uses much smaller sample of galaxies, and we find that our conclusions agree with those by Jones et al. (2017). Thus, we observe systematic growth of forbidden emission lines with respect to the Balmer lines from the gas with the altitude increasing. Also, we confirm the guess by Jones et al. that eDIG properties depend on some integral properties of the galaxies, e.g. on stellar mass and specific star formation rate.

We also notice that our results are in agreement with works by Belfiore et al. (2016), Zhang et al. (2017) that conclude that HOLMES are important for the DIG ionization. Unfortunately, direct comparison between our works is difficult because the galaxies considered by Belfiore et al. (2016), Zhang et al. (2017) allow them to study the DIG in the galactic midplanes only. The necessity of taking HOLMES into account for the description of the emission lines ratios in galactic gas is a significant addition to the previous assumption that OB-stars can explain the ratios in the majority of galaxies made by Haffner et al. (2009).

Promising conclusions were made in a study by Lacerda et al. (2018) based on panoramic spectroscopy results from the survey CALIFA. Lacerda et al. (2018) proposed to use the equivalent width (EW) of $H\alpha$ emission as an indicator of the gas ionization regime, i.e. to distinguish the gas in DIG from HII regions. A humble sample of edge-on galaxies demonstrated by Lacerda et al. (2018) gives a guess that the extraplanar gas is in the DIG ionization regime, too. We note that our approach to the gas analysis makes a reliable estimation of EWs difficult: while the flux from emission lines can be reliably measured even at the highest altitudes, the stellar continuum is not well detected very far away from the galactic midplane. We take the EW analysis out of the frames of our work.

At the end, we would like to discuss limitations of our approach to the gas state and ionization sources analysis at high galactic altitudes. Although the spectra stacking procedure helps us increase the range where the eDIG can be studied, the stacked spectra are contributed by galaxies of different kinds. The limited spatial resolution of MaNGA does not allow us to resolve individual HII regions in eDIG. We can only extrapolate our knowledge of smooth density distribution of gas at high galactic altitudes earned from studies of our Galaxy. We also note that we do not separate galaxies by dominating gas ionization mechanisms, e.g. by the presence of active galactic nuclei. Also, we do not consider any radial binning in this paper, which would help us check whether powerful central sources can contribute to the gas ionization. We also acknowledge a non-optimal determination of the vertical scale height of the disks via the effective radii. In this case, a two-dimensional photometric decomposition would allow us to determine the vertical disk scale more reliably and to eliminate inconsistencies for the case of galaxies with large bulges. We purposely prefer to estimate the vertical scale from the effective radius for this study in order to better compare results to the work by Jones et al. (2017). We postpone the possible adjustments to our analysis mentioned above to a future work.

CONCLUSIONS

We present results of a study of the ionization sources at different altitudes in galaxies of various types. The key element of this work is using a large sample of 239 true edge-on galaxies selected from a recent SDSS data release DR16, which allows us to study emission lines at extremely high altitudes via a spectra stacking procedure.

We compare the derived emission line ratios with results of modeling available from the 3MdB database, which enables us to consider the gas ionization by a combination of OB-stars and HOLMES, and also by shocks. We employ three BPT diagrams for the comparison.

We find that the model of gas ionization that takes into account two types of sources: OB-stars and HOLMES, adequately describes observed distributions of emission line ratios in galactic gas. Nevertheless, shock waves may be required for better description of DIG at high altitudes, especially at $z > 4.5 z_0$ in galaxies with intermediate and high stellar masses or with low specific star formation rates. Interaction of gas in galaxies with circumgalactic medium (see e.g. Slavin et al. 1993) can be a source of the shocks, which also affects the gas kinematics at high galactic altitudes (Bizyaev et al. 2022).

We infer how the OB-stars contribution to the total ionizing flux and the ionization parameter change with the altitude via the grid interpolation from the BPT diagrams and find the following trends:

- In the galaxies of all types (Figure 6) the contribution of OB-stars decreases, the contribution of HOLMES increases, and the ionization parameter decreases with the galactic altitude.
- The increasing of stellar mass (Figures 3 and 7) leads to the OB-contribution decreasing and HOLMES contribution increasing at any galactic altitudes. Also, the vertical gradient of the ionization parameter decreases in this case. In turn, at the highest galactic altitudes the stellar mass increasing leads to the increasing of the ionization parameter.
- At fixed low galactic altitudes the growth of the $H\alpha$ luminosity (Figures 4 and 8) leads to the increasing of OB-stars contribution and the decreasing of that from HOLMES. This trend blurs at higher altitudes.
- The most prominent difference in the considered sources of the gas ionization among all binning cases is seen for the galaxies with different specific star formation rates (Figures 5 and 9). With the specific star formation rate increasing, the OB-stars contribution increases and the one from HOLMES decreases. The ionization parameter vertical gradient also increases in this case. Moreover, for the galaxies with active star formation the contribution of OB-stars exceeds that from HOLMES at almost all galactic altitudes. In the star formation passive galaxies the OB-stars contribution is less than that from HOLMES at almost all galactic altitudes, and it does not change significantly with galactic altitude, as well as the ionization parameter.

ACKNOWLEDGEMENTS

This is a preprint of the work accepted for publication in *Astronomy Letters*, ©, copyright 2023, belonging to the authors, see <http://pleiades.online/>. This study was partly supported by the Russian Science Foundation via grant 22-12-00080, <https://rscf.ru/project/22-12-00080/>. The authors thank the anonymous referee for his constructive feedback that improved the paper.

The study makes use of the SDSS-IV MaNGA data available from http://www.sdss4.org/dr16/data_access/. The SDSS-IV website is <https://www.sdss4.org>. Funding for the Sloan Digital Sky Survey IV has been provided by the Alfred P. Sloan Foundation, the U.S. Department of Energy Office of Science, and the Participating Institutions. SDSS-IV acknowledges support and resources from the Center for High Performance Computing at the University of Utah.

SDSS-IV is managed by the Astrophysical Research Consortium for the Participating Institutions of the SDSS Collaboration including the Brazilian Participation Group, the Carnegie Institution for Science, Carnegie Mellon University, Center for Astrophysics — Harvard & Smithsonian, the Chilean Participation Group, the French Participation Group, Instituto de Astrofísica de Canarias, The Johns Hopkins University, Kavli Institute for the Physics and Mathematics of the Universe (IPMU) / University of Tokyo, the Korean Participation Group, Lawrence Berkeley National Laboratory, Leibniz Institut für Astrophysik Potsdam (AIP), Max-Planck-Institut für Astronomie (MPIA Heidelberg), Max-Planck-Institut für Astrophysik (MPA Garching), Max-Planck-Institut für Extraterrestrische Physik (MPE), National Astronomical Observatories of China, New Mexico State University, New York University, University of Notre Dame, Observatório Nacional / MCTI, The Ohio State University, Pennsylvania State University, Shanghai

Astronomical Observatory, United Kingdom Participation Group, Universidad Nacional Autónoma de México, University of Arizona, University of Colorado Boulder, University of Oxford, University of Portsmouth, University of Utah, University of Virginia, University of Washington, University of Wisconsin, Vanderbilt University, and Yale University.

REFERENCES

- Ahumada, R., Allende Prieto, C., Almeida, A., et al. 2020, *ApJS*, 249, 3
- Alarie, A., & Morisset, C. 2019, *Revista Mexicana de Astronomía y Astrofísica*, 55, 377
- Allen, M. G., Groves, B. A., Dopita, M. A., Sutherland, R. S., & Kewley, L. J. 2008, *ApJS*, 178, 20
- Andrews, B. H., & Martini, P. 2013, *ApJ*, 765, 140
- Baldwin, J. A., Phillips, M. M., & Terlevich, R. 1981, *PASP*, 93, 5
- Belfiore, F., Maiolino, R., Maraston, C., et al. 2016, *MNRAS*, 461, 3111
- Binette, L., Dopita, M. A., & Tuohy, I. R. 1985, *ApJ*, 297, 476
- Bizyaev, D., & Kajsins, S. 2004, *ApJ*, 613, 886
- Bizyaev, D. V., Kautsch, S. J., Mosenkov, A. V., et al. 2014, *ApJ*, 787, 24
- Bizyaev, D., Walterbos, R. A. M., Yoachim, P., et al. 2017, *ApJ*, 839, 87
- Bizyaev, D., Walterbos, R. A. M., Chen, Y.-M., et al. 2022, *MNRAS*, 515, 1598
- Blanton, M. R., Bershady, M. A., Abolfathi, B., et al. 2017, *AJ*, 154, 28
- Bundy, K., Bershady, M. A., Law, D. R., et al. 2015, *ApJ*, 798, 7
- Cappellari, M. 2017, *MNRAS*, 466, 798
- Cappellari, M., & Emsellem, E. 2004 *PASP*, 116, 138
- Collins, J. A., & Rand, R. J. 2001, *Gas and Galaxy Evolution, Astronomical Society of the Pacific Conference Proceedings*, 240 (Ed. Hibbard, J. E., Rupen, M., & van Gorkom, J. H., San Francisco: Astronomical Society of the Pacific), 392
- Curti, M., Cresci, G., Mannucci, F., et al. 2017, *MNRAS*, 465, 1384
- Dettmar, R.-J. 1990, *A&A*232, L15
- Dopita, M. A., Kewley, L. J., Heisler, C. A., & Sutherland, R. S. 2000, *ApJ*, 542, 224
- Dopita, M. A., Kewley, L. J., Sutherland, R. S., et al. 2016, *Ap&SS*, 361, 61
- Drory, N., MacDonald, N., Bershady, M. A., et al. 2015, *AJ*, 149, 77
- Ferland, G. J., Korista, K. T., Verner, D. A., et al. 1998, *PASP*, 110, 761
- Ferland, G. J., Porter, R. L., van Hoof, P. A. M., et al. 2013, *Revista Mexicana de Astronomía y Astrofísica*, 49, 137
- Flores-Fajardo, N., Morisset, C., Stasińska, G., & Binette L. 2011, *MNRAS*, 415, 2182
- Gunn, J. E., Siegmund, W. A., Mannery, E. J., et al. 2006, *AJ*, 131, 2332
- Haffner, L. M., Dettmar, R.-J., Beckman, J. E., et al. 2009, *Reviews of Modern Physics*, 81, 969
- Hao, C.-N., Kennicutt, R. C., Johnson, B. D., et al. 2011, *ApJ*, 741, 124
- Hoyle F., & Ellis, G. R. 1963, *Aust. J. Phys.*, 16, 1
- Jones, A., Kauffmann, G., D’Souza, R., et al. 2017, *A&A*, 599, A141
- Karachentsev, I. D., Makarov, D. I., & Kaisina, E. I. 2013, *AJ*, 145, 101
- Kauffmann, G., Heckman, T. M., Tremonti, C., et al. 2003, *MNRAS*, 346, 1055
- Kennicutt, R. C., & Evans, N. J. 2012, *ARA&A*, 50, 531
- Kewley, L. J., Dopita, M. A., Sutherland, R. S., et al. 2001, *ApJ*, 556, 121
- Kewley, L. J., Groves, B., Kauffmann, G., & Heckman T. 2006, *MNRAS*, 372, 961
- Lacerda, E. A. D., Cid Fernandes, R., Couto, G. S., et al. 2018, *MNRAS*, 474, 3727
- Law, D. R., Yan, R., Bershady, M. A., et al. 2015, *AJ*, 150, 19
- Law, D. R., Cherinka, B., Yan, R., et al. 2016, *AJ*, 152, 83
- Law, D. R., Ji, X., Belfiore, F., et al. 2021, *ApJ*, 915, 35
- Levy, R. C., Bolatto, A. D., Sánchez, S. F., et al. 2019, *ApJ*, 882, 84
- Licquia T. C., & Newman J. A. 2015, *ApJ*, 806, 96
- Marasco, A., Fraternali, F., & Heald, G. 2019, *A&A*, 631, 50
- Masters, D., Faisst, A., & Capak, P. 2016, *ApJ*, 828, 18
- McMillan, P. J. 2017, *MNRAS*, 465, 76
- Moiseev, A. V., Smirnova, K. I., Smirnova, A. A., & Reshetnikov V. P. 2011, *MNRAS*, 418, 244
- Morisset, C., Delgado-Inglada, G., & Flores-Fajardo, N. 2015, *Revista Mexicana de Astronomía y Astrofísica*, 51, 103
- Mosenkov, A. V., Sotnikova, N. Ya., Reshetnikov, V. P., et al. 2015, *MNRAS*, 451, 2376
- Murphy, E. J., Condon, J. J., Schinnerer, E., et al. 2011, *ApJ*, 737, 67
- Pérez-Montero E., & Contini, T. 2009, *MNRAS*, 398, 949
- Rand, R. J. 2000, *ApJ*, 537, L13
- Rand, R. J., Kulkarni, S. R., & Hester, J. J. 1990, *ApJL*, 352, L1
- Reynolds, R. J., Scherb, F., & Roesler, F. L. 1973, *ApJ*, 185, 869
- Reynolds, R. J. 1991, *The Interstellar Disk-Halo Connection in Galaxies*, IAU Symp., 144 (Ed. Bloemen H., Dordrecht: Kluwer Acad. Publ.), 67
- Robitaille T. P., & Whitney, B. A. 2010, *ApJL*, 710, L11
- Shaw M. A., & Gilmore, G. 1989, *MNRAS*, 237, 903
- Slavin, J. D., Shull, J. M., & Begelman M. C. 1993, *ApJ*, 407, 83
- Smee, S. A., Gunn, J. E., Uomoto, A., et al. 2013, *AJ*, 146, 32
- Sutherland, R., Dopita, M., Binette, L., & Groves, B. 2018, "MAPPINGS V: Astrophysical plasma modeling code", *Astrophysics Source Code Library*, ascl:1807.005
- Swaters, R. A., Sancisi, R., & van der Hulst J. M. 1997, *ApJ*, 491, 140
- Tremonti, C. A., Heckman, T. M., Kauffmann, G., et al. 2004, *ApJ*, 613, 898
- Veilleux S., & Osterbrock, D. E. 1987, *ApJS*, 63, 295
- Wake, D. A., Bundy, K., Diamond-Stanic, A. M., et al. 2017, *AJ*, 154, 86
- Westfall, K. B., Cappellari, M., Bershady, M. A., et al. 2019, *AJ*, 158, 231
- Yan, R., Bundy, K., Law, D. R., et al. 2016, *AJ*, 152, 197
- Yan, R., Tremonti, C., Bershady, M. A., et al. 2016, *AJ*, 151, 8
- York, D. G., Adelman, J., Anderson, J. E., et al. 2000, *AJ*, 120, 1579
- Zhang, K., Yan, R., Bundy, K., et al. 2017, *MNRAS*, 466, 3217